

Uncertainty Quantification of Spalart–Allmaras Turbulence Model Coefficients for Simplified Compressor Flow Features

Xiao He¹

Department of Mechanical Engineering,
Imperial College London,
London SW7 2AZ, UK
e-mail: xiao.he2014@imperial.ac.uk

Fanzhou Zhao

Department of Mechanical Engineering,
Imperial College London,
London SW7 2AZ, UK

Mehdi Vahdati

Department of Mechanical Engineering,
Imperial College London,
London SW7 2AZ, UK

Turbulence model in Reynolds-averaged Navier–Stokes (RANS) simulations has a crucial effect on predicting the compressor flows. In this paper, the parametric uncertainty of the Spalart–Allmaras (SA) turbulence model is studied in simplified two-dimensional (2D) flows, which includes some of the compressor tip flow features. The uncertainty is quantified by a metamodel-based Monte Carlo method. The model coefficients are represented by uniform distributions within intervals, and the quantities of interest include the velocity profile, the Reynolds stress profile, the shock front, and the separation size. An artificial neural network (ANN) is applied as the metamodel, which is tuned, trained, and tested using databases from the flow solver. The uncertainty of quantities of interest is determined by the range of the metamodel and the database samples from the flow solver. The sensitivity of the model coefficients is quantified by calculating the gradient of quantities of interest from the metamodel. Results show that the high-fidelity data of the quantities of interest cannot be fully enveloped by the uncertainty band in regions with separation and shock. Crucial model coefficients on the quantities of interest are identified. However, recalibration of these coefficients results in contradictory prediction of different quantities of interest across flow regimes, which indicates the need for a modified Spalart–Allmaras turbulence model form to improve the accuracy in predicting complex flow features. [DOI: 10.1115/1.4047026]

1 Introduction

Reliability is of most importance for gas turbine compressors. A conventional approach to analyze compressor stability is to solve the Reynolds-averaged Navier–Stokes (RANS) equations with a turbulence model for closure. The Spalart–Allmaras (SA) turbulence model [1] is one of the most popular turbulence models in compressor aerodynamics due to its robustness and high numerical efficiency. Through the combined RANS-SA approach, understandings toward physics of compressor aerodynamic instability were advanced: unsteady flow fields during the surge [2] and rotating stall [3,4] cycles were visualized, and vortical structures that lead to the stall inception were identified [5]. However, since the SA model is designed and calibrated in simple free shear flows and wall-bounded flows, it shows low accuracy in compressor near-stall flows [6,7] and often fails to predict the compressor stall margin accurately.

With the rapid development of data science, techniques such as uncertainty quantification (UQ) have brought new horizons and renewed interest in the field of turbulence modeling [8]. The purpose of conducting UQ studies on turbulence models is not to design a perfect model form that best fits the nature of turbulence; instead, it is to evaluate the level of confidence in results obtained by using an existing model that has intrinsic flaws. Origin of uncertainties in RANS turbulence models can be classified into model-form uncertainties and parametric uncertainties. The model-form uncertainties arise from assumptions that determine the mathematical form of the model (e.g., the Boussinesq approximation). The parametric uncertainties come from the model

coefficients that are calibrated by a limited number of simple flow cases. Both types of uncertainties are epistemic.

One of the pioneering UQ works on the SA turbulence model is from Godfrey and Cliff [9]. They built intrusive sensitivity equations to analyze the sensitivities of SA model coefficients for predicting a subsonic flat plate boundary layer. It was concluded that the SA model coefficients c_{v1} , c_{b1} , σ , and c_{w2} are most influential, but no information about the uncertainty of results was obtained. Later research quantifies uncertainties through either a forward or a backward propagation framework [10].

The forward approach pre-assumes the probability density function (PDF) of model terms or model coefficients and then propagates it through RANS equations to obtain the PDF of the quantity of interest (QoI). An example of the forward approach is from Han and Hosder [11], where the model-form uncertainty of the SA model was investigated by multiplying the eddy viscosity by a random variable with a uniform PDF. In their study, the measured velocity profiles of the synthetic jet actuator case could be enveloped by the 95% confidence interval. Another example is from Schaefer et al. [12,13] and Stephanopoulos et al. [14], where the nonintrusive polynomial chaos method was applied to investigate the parametric uncertainty of the SA model. The idea was to train a metamodel of RANS equations based on the response surface and then propagate the SA model coefficients with uniform PDFs through the metamodel. Their test cases included the transonic axisymmetric bump, the RAE 2822 transonic airfoil, the subsonic flat plate, and the subsonic backward-facing step. It was generally found that the discrepancy between the experiment and the simulation was most evident in the separation regions, and the predicted results were sensitive to the SA model coefficients σ , κ , c_{v1} , c_{b1} , and c_{w2} .

The backward approach first solves a calibration problem in a Bayesian framework, which utilizes high-fidelity (hi-fi) data to infer a proper PDF of model terms or model coefficients. The calibrated PDF is then propagated to predict the PDF of the QoI.

¹Corresponding author.

Contributed by the Fluids Engineering Division of ASME for publication in the JOURNAL OF FLUIDS ENGINEERING. Manuscript received November 8, 2019; final manuscript received March 26, 2020; published online May 11, 2020. Assoc. Editor: Sergio Pirozzoli.

Oliver and Moser [15] calibrated the SA model coefficients in a fully developed channel flow, and the calibrated coefficients σ and κ have very similar values to their defaults. An ensemble Karman filter method was proposed by Kato and Obayashi [16] to calibrate the SA model coefficients, which reproduced the default coefficient values in a zero-pressure gradient flat plate flow. Cheung et al. [17] performed a calibration of SA model coefficients in a subsonic flat plate under different pressure gradients, and an evident difference between default values and calibrated values of SA model coefficients was observed for all calibration scenarios. Similar calibrations in flat plate flows have been performed by Edeling et al. [18], but no general set of coefficient values can be found for all cases under different pressure gradients. Papadimitriou and Papadimitriou [19] adopted an adjoint method to optimize the posterior Gaussian distribution of the SA model coefficients. Calibration and prediction in the subsonic flat plate and the subsonic backward-facing step case was conducted, and the SA model was found accurate except for the separation region.

Previous researches reviewed above have investigated the uncertainty and the sensitivity of SA model coefficients on certain QoIs and flow regimes, and recalibration of SA model coefficients improved the model accuracy in certain cases. Is it possible to improve the prediction on different compressor flow features simultaneously by recalibrating the coefficients? Which model coefficient or model term needs the most attention for future model modifications? In an attempt to answer these questions, an efficient forward-propagation UQ framework is applied to investigate simplified two-dimensional (2D) compressor flow features. The choice of the 2D flows will be clarified first, followed by the detailed introduction to the flow solver, the UQ method, and the metamodel. Finally, uncertainties in velocity profiles, Reynolds stress, shock, and separation will be discussed, respectively.

2 Methodology

2.1 Extraction of Compressor Flow Features. The corner between the casing wall and the blade suction surfaces at the tip is the dominant region for determining the compressor performance [20]. The tip flow of a transonic compressor is dominated by the interaction between the shock, the boundary layer, and the tip leakage flow, which is highly three-dimensional in nature. The tip leakage flow illustrated in Fig. 1(a) produces significant turbulent kinetic energy and thus increases endwall viscous losses [21]. The shock structure presented in Fig. 1(b) induces boundary layer separation that enhances the blockage and the efficiency loss [22]. The tip leakage flow and the shock structure are highly interactive. When a transonic compressor operates toward the stall limit, the tip leakage vortex breakdown occurs after the shock front, which leads to the compressor stall [23–25].

In this paper, simplified 2D flows, namely, the backward-facing step flow (Fig. 1(c)) and the axisymmetric transonic bump flow (Fig. 1(d)), are investigated for the UQ study. These flows share similar flow physics to the tip leakage flow and the

shock-boundary layer interaction, and they represent the least challenging cases for the evaluation of turbulence models on compressor tip flow features. An advantage of studying the simplified two-dimensional flows is a better understanding on the capability of SA model, as it decouples features of the tip leakage flow and the shock-boundary layer interaction. Another merit of this approach is the easy access to the hi-fi data including Reynolds stress, shock location and strength, and separation size, which are not readily available for high-speed compressor rotors. However, it should be emphasized that the main physics of compressor tip flow is highly three-dimensional, which cannot be fully represented by the 2D cases studied. Thus, accurate prediction of the simplified 2D flows is necessary but may not be sufficient for the accurate prediction of the compressor tip flow features.

In the following discussions, the UQ results will be compared with the experimental data of the step flow [26] and the bump flow [27,28]. Results from hi-fi simulations are also employed for reference, including the improved delayed detached eddy simulation for the step flow [29] and the wall-resolved large eddy simulation for the bump flow [30]. For consistency and simplicity, both hi-fi simulations are referred to as the large eddy simulation (LES) results.

2.2 The Spalart–Allmaras Turbulence Model. The SA turbulence model [1] is a linear eddy viscosity model based on the Boussinesq approximation as follows:

$$\tau_{ij} = 2\mu_t \left(S_{ij} - \frac{1}{3} \frac{\partial u_k}{\partial x_k} \delta_{ij} \right) \quad (1)$$

where the turbulent shear stress τ_{ij} is linearly correlated with the mean strain rate S_{ij} , and the turbulent viscosity μ_t is solved by the following equation:

$$\mu_t = \rho \hat{\nu} f_{v1} \quad (2)$$

The modified turbulent viscosity $\hat{\nu}$ is solved by the transport equation shown in the following equation:

$$\begin{aligned} \frac{\partial \hat{\nu}}{\partial t} + u_j \frac{\partial \hat{\nu}}{\partial x_j} = & \underbrace{\left[c_{b1} (1 - f_{t2}) \hat{S} \hat{\nu} \right]}_{\text{production}} - \underbrace{\left[c_{w1} f_w - \frac{c_{b1}}{\kappa^2} f_{t2} \right] \left(\frac{\hat{\nu}}{d} \right)^2}_{\text{destruction}} \\ & + \underbrace{\frac{1}{\sigma} \left[\frac{\partial}{\partial x_j} \left((\nu + \hat{\nu}) \frac{\partial \hat{\nu}}{\partial x_j} \right) + c_{b2} \frac{\partial \hat{\nu}}{\partial x_i} \frac{\partial \hat{\nu}}{\partial x_i} \right]}_{\text{diffusion}} \end{aligned} \quad (3)$$

where the modified strain rate \hat{S} is defined as follows:

$$\hat{S} = \Omega + \frac{\nu}{\kappa^2 d^2} \chi f_{v2} \quad (4)$$

and additional variables are calculated in Eq. (5) using coefficients summarized in Table 1. Among these equations, ρ is the density, Ω is the vorticity magnitude, and d is the wall distance

$$\begin{aligned} c_{w1} &= \frac{c_{b1}}{\kappa^2} + \frac{1 + c_{b2}}{\sigma} & f_{v1} &= \frac{\chi^3}{\chi^3 + c_{v1}^3} & \chi &= \frac{\hat{\nu}}{\nu} \\ f_{v2} &= 1 - \frac{\chi}{1 + \chi f_{v1}} & f_w &= g \left[\frac{1 + c_{w3}^6}{g^6 + c_{w3}^6} \right]^{1/6} \\ g &= r + c_{w2}(r^6 - r) & r &= \min \left[\frac{\hat{\nu}}{\chi \kappa^2 d^2}, 10 \right] \\ f_{t2} &= c_{t3} \exp(-c_{t4} \chi^2) \end{aligned} \quad (5)$$

In this paper, all the SA model coefficients are investigated except for transition-related terms c_{t3} and c_{t4} . The physical relevance and the investigated interval of the SA model coefficients are shown in Table 1. The intervals of coefficients were verified by Spalart as reported in Schaefer et al. [12], which arose from the

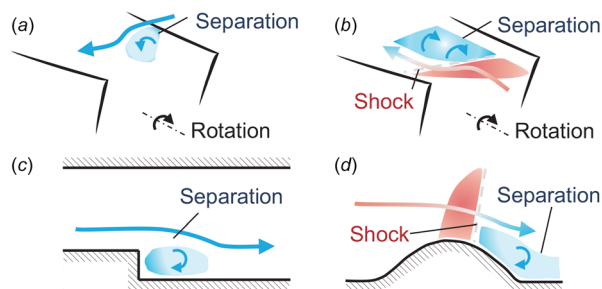
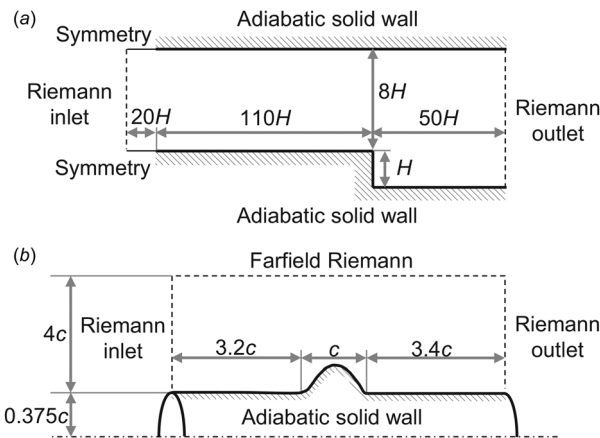


Fig. 1 Illustration of (a) compressor tip leakage flow, (b) compressor shock-boundary layer interaction, (c) backward-facing step flow, and (d) axisymmetric transonic bump flow

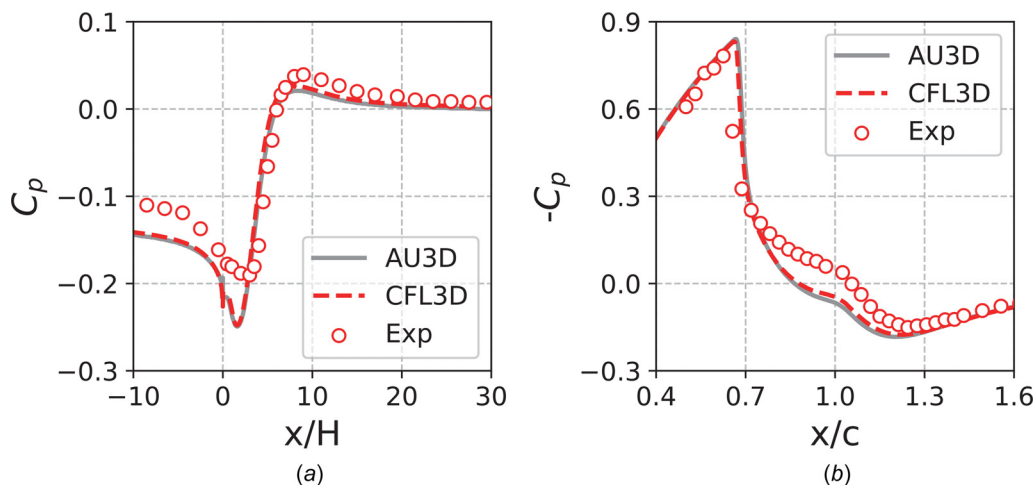
Table 1 Range of Spalart–Allmaras turbulence model coefficients studied

Coefficient	Physical relevance	Minimum	Default	Maximum
σ	Diffusion coefficient	0.600	0.667	1.000
k	Log law slope	0.38	0.41	0.42
c_{v1}	Log law intercept	6.9	7.1	7.3
c_{b1}	Production coefficient	0.128	0.1355	0.137
c_{b2}	Conserve $\nu_1^{1+c_{b2}}$	0.609	0.622	0.688
c_{w2}	Calibrate skin friction	0.055	0.300	0.353
c_{w3}	Speed up destruction	1.75	2.00	2.50

**Fig. 2 Geometry and boundary conditions for (a) backward-facing step flow and (b) axisymmetric transonic bump flow****Table 2 Mesh size and operating conditions**

Case	Mesh size	Re	Ma	$T(K)$
Step	$2 \times 354 \times 257$	3.6×10^4	0.15	298.33
Bump	$2 \times 721 \times 321$	2.763×10^6	0.875	300

calibration process concerning free shear flows and simple wall-attached flows [1]. Using coefficients beyond these intervals will result in poor predictions on these calibration flows. Thus, coefficient values beyond these intervals are not studied in the paper.

**Fig. 3 Validation and verification on surface pressure coefficient of (a) step and (b) bump (experiment data: Refs. [26] and [28]; CFL3D data: Ref. [33])**

2.3 Flow Solver, Validation, and Verification. The in-house computational fluid dynamics (CFD) solver AU3D solves the three-dimensional, viscous and compressible RANS equations based on a cell-vertex finite volume scheme. The numerical fluxes are solved by the Jameson–Schmidt–Tukel scheme with artificial viscosity based on Roe’s matrix, and the second-order accuracy in space is achieved in all parts of computation domain except for the vicinity of shocks by using a pressure switch. For steady simulations, the time stepping is based on a point-implicit scheme with Jacobian iterations. Techniques including residual smoothing and local time stepping are adopted to accelerate convergence. The solver has been used for solving the flows in compressors for more than 20 years with a good degree of success [2,3]. More details of the solver can be found in Sayma et al. [31].

Boundary conditions used for the step case and the bump case are presented in Fig. 2. The wall boundaries are set as the adiabatic solid walls. The inlet, outlet, and farfield are set as Riemann boundary conditions [32]. The periodic boundary is set as symmetry. Mesh size and operating conditions are summarized in Table 2. The meshes in use were verified by AU3D to produce mesh independent results. These meshes are the second finest provided by the turbulence modeling resource website [33]. Steady RANS simulations are performed throughout the paper.

In Fig. 3, the surface pressure coefficient is plotted against the axial distance normalized by the step height (H) or the bump chord length (c). To verify the implementation of the original Spalart–Allmaras (OSA) model, the results from AU3D are compared to that from the NASA code CFL3D [33]. It is illustrated that the AU3D results overlap with that from CFL3D, indicating that the implementation is correct. An evident difference between experiments and both simulations is also captured, which illustrates the deficiency of the OSA model.

2.4 Uncertainty Quantification Method. Conventional UQ methods like Monte Carlo are computationally intensive to approximate the solution with high accuracy. In this paper, the parametric uncertainty of SA model coefficients is investigated through a metamodel-based Monte Carlo approach so that the required numerical resources can be alleviated. This framework is illustrated in Fig. 4.

First, the Latin Hypercube sampling method [34] is applied to generate five independent databases of SA model coefficient sets within the intervals in Table 1. This design of experiment method is able to distribute the samples as uniformly as possible in the investigated space. The database size is 16, 32, 64, 128, and 256, respectively, which will be referred to as $db1$ to $db5$ in the following discussions. In the first place, it was verified that all of the five

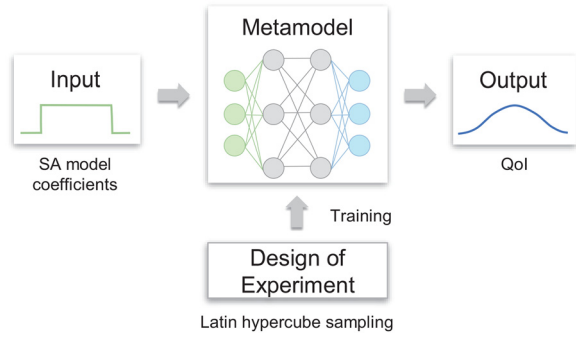


Fig. 4 Illustration of the metamodel-based uncertainty quantification framework

databases are mutually independent, since the minimum Euclidean distance between arbitrary two samples from different databases ranges from 7% to 25% of the longest distance in the domain (i.e., $\sqrt{7}$).

The generated databases are then applied to train and test a metamodel of CFD. The metamodel is a reduced-order model that directly links the input variables with QoIs without solving RANS equations

$$\hat{\mathbf{q}} \approx \mathbf{q} \equiv \mathbf{M}(\mathbf{x}) \quad (6)$$

where \mathbf{x} is the vector of input variables, $\mathbf{M}(\cdot)$ denotes the metamodel, and $\hat{\mathbf{q}}$ and \mathbf{q} are the vector of QoIs from CFD and the metamodel, respectively.

Finally, the uncertainty of QoIs can be quantified by the maximum and the minimum values predicted by the metamodel. The PDF of QoIs can be obtained when the PDF of input variables is known. In this work, the SA model coefficients are assumed to have a uniform distribution. The global sensitivity of input variables on predicting QoIs can be quantified by the mean gradient calculated from the metamodel, as defined in the following equation:

$$\frac{\partial \overline{M}_i}{\partial \hat{x}_j} = \underbrace{\left[\dots \right]}_{nx} \frac{\partial M_i}{\partial \hat{x}_j} d\hat{x}_1 \dots d\hat{x}_{nx} \quad (7)$$

where \hat{x}_j is the input variable normalized to the range of $[0, 1]$, and n_x is the dimension of the input vector. To compare the sensitivity among different QoIs, the mean gradient will be normalized by the length of the mean gradient vector $|\nabla \overline{M}_i|$. This term will be referred to as normalized gradient in the following discussion.

2.5 Metamodel Based on Artificial Neural Network. In this study, the artificial neural network (ANN) is applied to construct a metamodel of the CFD solver. The ANN is a well-established reduced-order model in a broad range of thermofluids applications [35–37]. The mathematical form and the working principle of the ANN are detailed below.

2.5.1 Artificial Neural Network Representation. The ANN is composed of multiple levels of artificial neurons, as illustrated in Fig. 5. The input variables, the intermediate values, and the QoIs are stored in the input layer, hidden layers, and the output layer, respectively. In this case, the SA model coefficients are fed in the input layer, and the QoIs including the Reynolds stress (τ_{xy}), the shock front location (x_{sf}), the pressure coefficient ($-C_{psf}$), the separation size (L_s), and the velocity (u_x) are imposed at the output layer. The shock front is defined as the location with the lowest wall pressure; the separation size is defined as the distance between the separation and the reattachment points. Separate

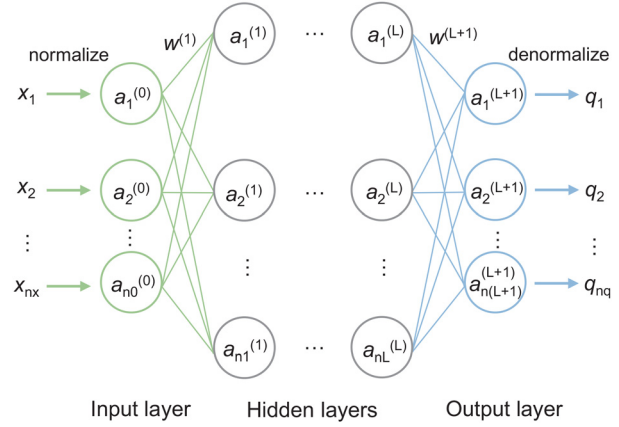


Fig. 5 Architecture of artificial neural network

Table 3 Details of metamodels for different quantities of interest

QoI group	n_q	Outputs	Figures
Velocity profile	8	$u_x(y_i)$	7, 8, and 9
Reynolds stress profile	8	$\tau_{xy}(y_i)$	7, 8, and 10
Reynolds stress	1	$\tau_{xy}(x, y)$	11 and 12
Shock	2	$x_{sf}, -C_{psf}$	7, 8, 13, 14, and 16
Separation	1	L_s	7, 8, 15, 16, and 17

ANN metamodels are constructed for each group of QoIs in each flow case, as detailed in Table 3.

2.5.2 Prediction by Forward Propagation. The ANN predicts the QoIs by the following steps. First, the SA model coefficients are normalized by their maximum and minimum values (i.e., min–max normalization) presented in Table 1. The values at the l th layer are then propagated to the $(l+1)$ th layer using the following equation:

$$\mathbf{a}^{(l+1)} = g(\mathbf{w}^{(l+1)} \mathbf{a}^{(l)} + \mathbf{b}^{(l+1)}) \quad (8)$$

where \mathbf{w} is the weight matrix, \mathbf{b} is the bias vector, and $g(\cdot)$ is the activation function. Here, the nonlinear sigmoid function is used as the activation function. Since the output of the sigmoid function ranges from 0 to 1, the values at the output layer need to be denormalized back to the values of the QoIs. The minimum and maximum values of the QoIs in the training database are used for normalization. Considering the QoIs from the test database may fall out of the training database range, the QoIs are normalized to the range of $0.5 \pm 0.5\omega^{-1}$, where ω is a scale factor. When $\omega = 1$, it turns back to the min-max normalization. The prediction accuracy of the ANN can be measured by the normalized error defined by the following equation:

$$\varepsilon = \frac{1}{m} \frac{1}{n_q} \sum_{j=1}^m \sum_{i=1}^{n_q} \frac{|q_i^{(j)} - \hat{q}_i^{(j)}|}{\max_{1 \leq k \leq m_{tr}} \hat{q}_i^{(k)} - \min_{1 \leq k \leq m_{tr}} \hat{q}_i^{(k)}} \times 100\% \quad (9)$$

2.5.3 Learning With Backpropagation. The accuracy of the ANN depends on the network parameters $\mathbf{w}^{(l)}$ and $\mathbf{b}^{(l)}$, which are initialized randomly before training. Calibration of these parameters, or training of the ANN, is achieved by solving an optimization problem that minimizes the cost function J defined by the following equation:

$$J(w_{i,k}^{(l)}, b_i^{(l)}) = \frac{1}{2m} \sum_{j=1}^m \sum_{i=1}^{n_{L+1}} (q_i^{(j)} - \hat{q}_i^{(j)})^2 + \frac{\lambda}{2m} \sum_{l=1}^{L+1} \sum_{i=1}^{n_l} \sum_{k=1}^{n_{l-1}} (w_{i,k}^{(l)})^2 \quad (10)$$

where λ is a regularization factor that penalizes large-valued weights in order to avoid overfitting. In this paper, the gradient-based Broyden–Fletcher–Goldfarb–Shanno optimizer [38] is applied, and the gradient of the cost function is calculated by the backpropagation algorithm. An example of the learning process is given in Fig. 6, where the training and test errors are plotted against the optimization epochs. Convergence of the optimization algorithm can be achieved before reaching the maximum iteration of 5000. It should be noted that the gradient-based optimization methods may lead to a local optimum result rather than the global optimum. To reduce the chance of falling into a local optimum, 16 ANNs with different initial conditions are trained parallelly, and the best ANN is chosen.

2.5.4 Hyperparameter Study. In addition to the standard parameters that can be learned from the training database, there are some hyperparameters that need to be determined before the learning process, namely, the number of hidden layers (L), the number of artificial neurons in each hidden layer (n_L), the scale factor (ω), and the regularization factor (λ). A parametric study of n_1 , ω , and λ has been conducted by changing one hyperparameter at a time while keeping the others at the baseline setting, which is $L = 1$, $n_1 = 0.5(n_x + n_q)$, $\omega = 2$, and $\lambda = 10^{-4}$. The prediction errors of ANNs in various QoIs are plotted against each hyperparameter in Fig. 7. It is observed that, with one hidden layer, the baseline setting of the hyperparameters leads to a high-accuracy ANN model (i.e., $\varepsilon < 2\%$). Increasing the number of hidden layers can potentially improve the accuracy further, but the required amount of training data needs to be increased in order to avoid overfitting. Considering the balance between the model accuracy and the cost, the baseline setting is adopted throughout the paper.

2.5.5 Training Data Independence Study. The training database size has a crucial effect on the accuracy of a metamodel. A rule of thumb for the minimum training database size is $m_{\min} = 10n_x$, which yields $m_{\min} = 70$ in this study. However, this rule of thumb does not consider the complexity of the metamodel and thus may underestimate the value of m_{\min} . Another approach to estimate m_{\min} is to consider that the number of equations (i.e., training data) should surpass the number of unknowns (i.e., ANN parameters). For an ANN with one hidden layer, this leads to $m_{\min} = (n_x n_1 + n_1 n_q + n_1 + n_q)/n_q$, which yields $m_{\min} = 37$ for all ANNs listed in Table 3.

To further analyze the effect of training database size, a training data independence study has been performed by using different

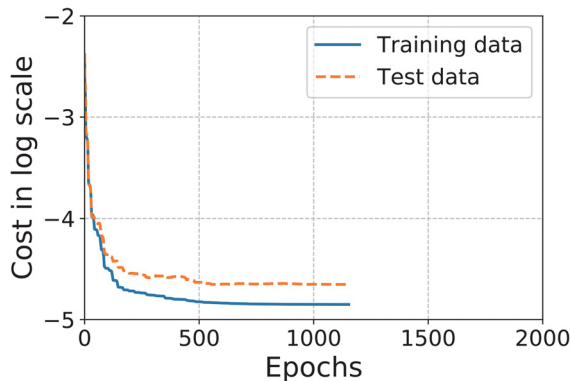


Fig. 6 Training history (output: L_s of bump; training data: $db5$; test data: $db4$)

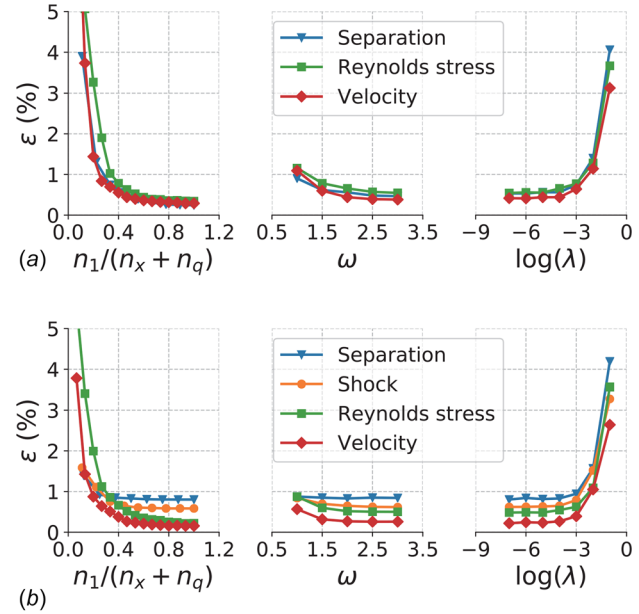


Fig. 7 Hyperparametric study: (a) backward-facing step and (b) axisymmetric transonic bump (training data: $db5$; cross-validation data: the union of $db1$, $db2$, and $db3$)

combinations of databases to train and test the ANN. The training and the test database are $db\{i\}$ and $db\{i-1\}$, respectively, so that the ratio of training database size to test database size can be kept the same as 2. When increasing the training database size, the difference between the test and training errors (i.e., ε_{te} and ε_{tr}) reduces to zero, and thus, the accuracy of the ANN model becomes independent of the training database size. It is confirmed in Fig. 8 that using the training database size of 256 achieves a data-independent result, where the differences between ε_{te} and ε_{tr} are below 0.3%. Hence, the $db5$ with 256 samples has been chosen to train ANNs in the following discussions.

3 Results

3.1 Uncertainty in Velocity Profiles. In the first step, the flow physics of the step case and the bump case is briefly introduced using the velocity profiles illustrated in Fig. 9. In these plots, the solid lines are RANS results using the SA model, the dotted lines represent the LES simulations, the dashed lines denote the min–max bounds predicted by the ANN, and the open circles represent the experimental data.

For the step case shown in Fig. 9(a), a shear layer indicated by the high velocity gradient is generated right after the step at Sec. I. A separation bubble is also formed beneath the shear layer, which is captured by the change of velocity orientation in the lower parts of Secs. I and II. Comparing the results from the SA model with the hi-fi data, the major deficiency is found at Sec. I, where the flow just separates from the step wall. In other sections, the hi-fi data can be generally enveloped by the uncertainty band of the velocity profile. An exception occurs in the near-wall region at Sec. IV, where the SA model underpredicts the velocity gradient and thus the local skin friction.

For the bump case presented in Fig. 9(b), the primary flow physics is the shock-induced flow separation. The shock front is located near Sec. I, which results in the wide uncertainty band of the local velocity profile. When passing through the shock, a separation bubble is formed at the trailing edge corner of the bump, which is captured by the reverse flow in the lower parts of Secs. II–V. The uncertainty bands are still evident at these sections inside the separation bubble. When the flow reattaches at Secs. VI and VII, the uncertainty in velocity profile reduces.

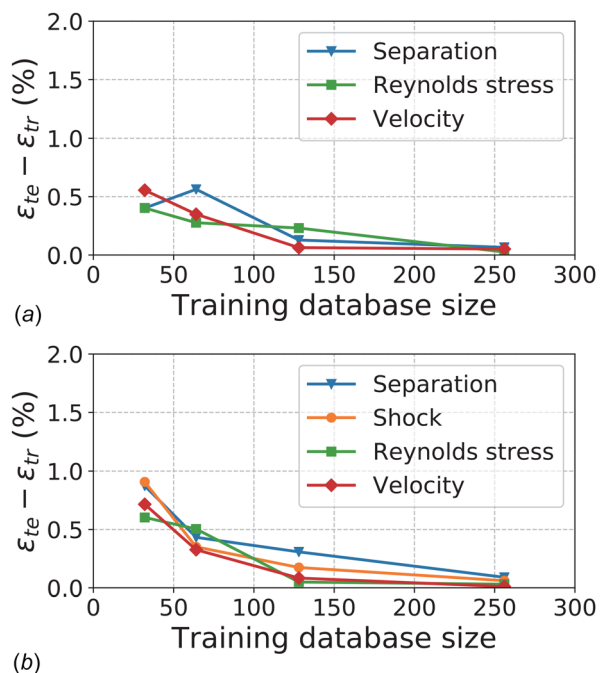


Fig. 8 Training data independence study: (a) backward-facing step and (b) axisymmetric transonic bump

Compared to the results from the SA model, the measured data fall within the uncertainty band, but the LES data do not. This is due to the early shock formation in LES, which will be presented later in Sec. 3.3.

3.2 Uncertainty in Reynolds Stress Prediction. The Reynolds stress profiles of the step case are shown in Fig. 10(a). It is observed that the hi-fi data overlap with the uncertainty band when the flow just detaches from the step at Sec. I. As the flow develops to Sec. II, the SA model underpredicts the downward advection of the peak of the Reynolds stress profile. Consequently, the hi-fi results cannot be fully enveloped by the uncertainty band. At Sec. III, the uncertainty band converges to the profile predicted by the SA model, but the deficiency still exists. When the flow is reattached at Sec. IV, the hi-fi data become closer to the results from the SA model again. These observations indicate that the uncertainty and deficiency of the SA model become evident in the separated region.

The Reynolds stress profiles of the bump case are presented in Fig. 10(b). Similar observations can be made: the uncertainty of the Reynolds stress and the discrepancy between the SA model results and the hi-fi results are much higher in the shock region near Sec. I and the separated region from Secs. II–VI than elsewhere. Moreover, the peak values of the Reynolds stress profiles are underpredicted by the SA model. It should be noted that the strain rate downstream of the bump mainly depends on the shock-induced separation strength. An accurate prediction of the shock

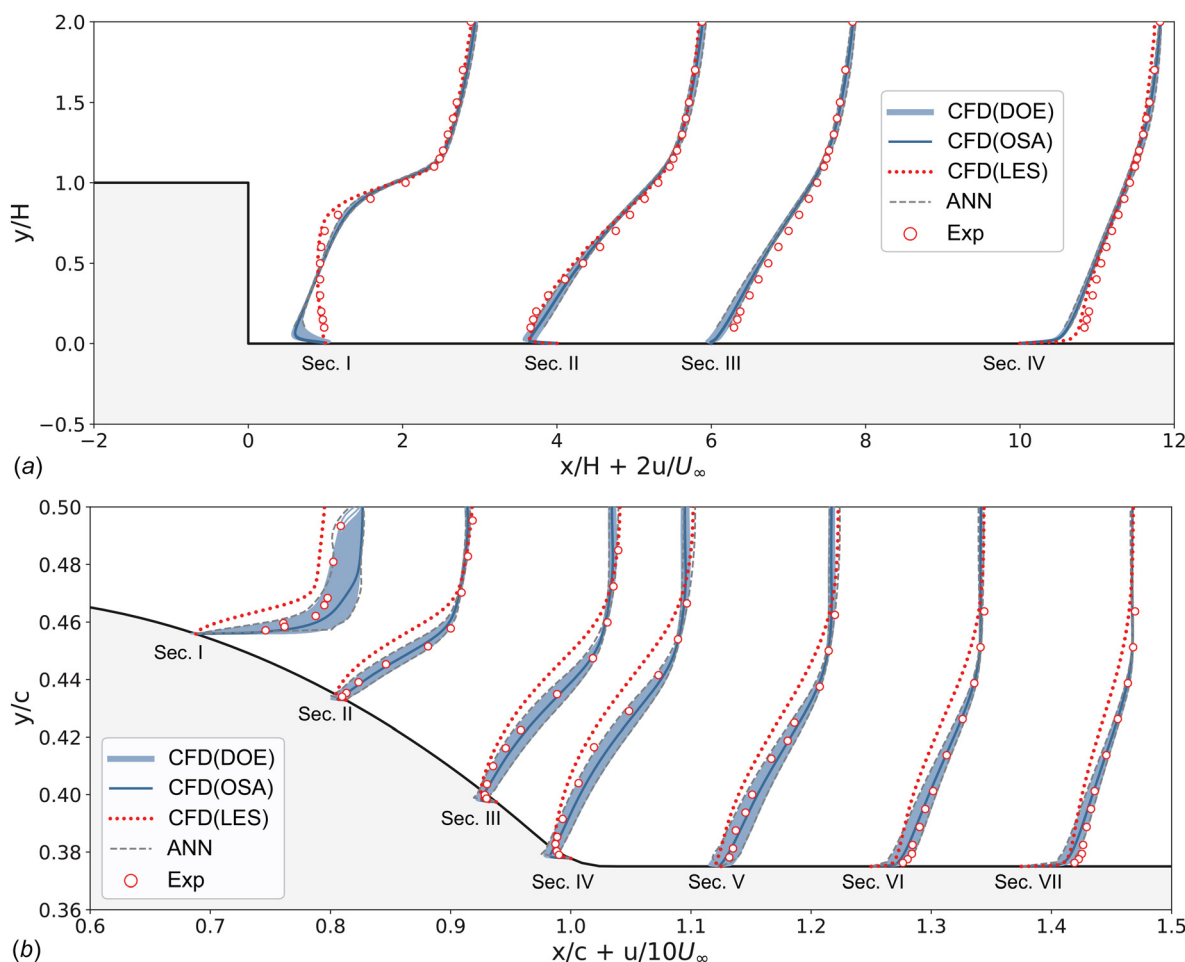


Fig. 9 Uncertainty of predicted velocity profiles: (a) backward-facing step and (b) axisymmetric transonic bump (experiment data: Refs. [26] and [28]; LES data: Refs. [29] and [30])

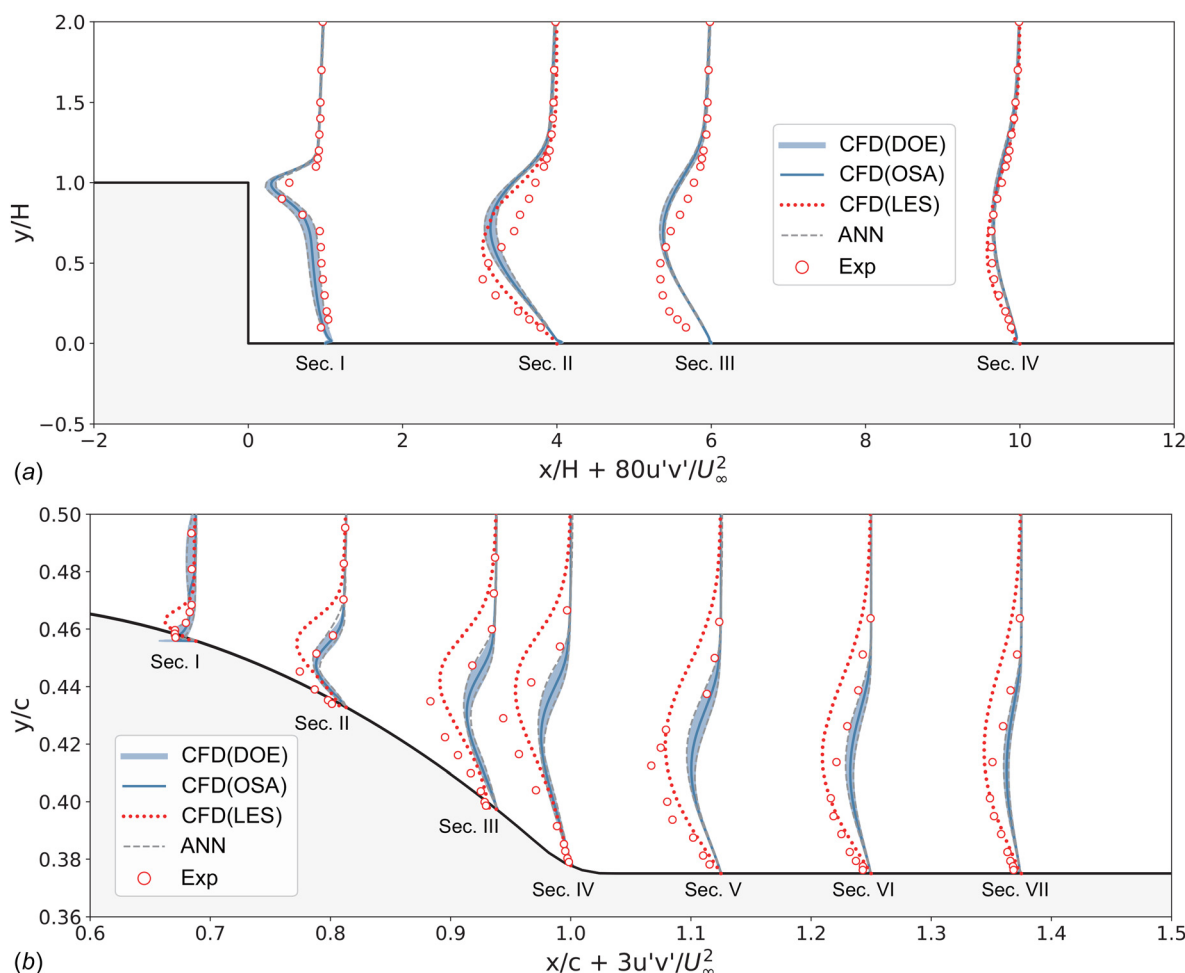


Fig. 10 Uncertainty of predicted Reynolds stress profiles: (a) backward-facing step and (b) axisymmetric transonic bump (bump experiment data: Refs. [26] and [28]; bump LES data: Refs. [29] and [30])

front location and the separation size is a prerequisite for predicting the Reynolds stress field correctly.

The sensitivity analyses on predicting the Reynolds stress field of the step flow are performed in Fig. 11. The contour shown in these figures represents the mean gradient of Reynolds stress with respect to each SA model coefficient, which is nondimensionalized by the mainstream velocity and the coefficient interval. This gradient at each mesh point is calculated by a separate ANN model. In general, the SA model coefficients σ , κ , c_{b1} , and c_{w2} have significant effects, while c_{v1} , c_{b2} , and c_{w3} are negligible and thus not shown here. The most sensitive region of the step flow is the separation bubble. Increasing the coefficient σ reduces the turbulence diffusion term, which increases the Reynolds stress in the separation region and decreases the Reynolds stress in the nearby upper and lower regions. The coefficient σ also exists in the c_{w1} term of the turbulence destruction term. An increase in σ will reduce the near-wall turbulence destruction, decrease the need for turbulence diffusion to the walls, and thus increase the Reynolds stress level in the separation region. The coefficient κ exists in \hat{S} of the turbulence production term and c_{w1} and f_w of the turbulence destruction term. The net source term related to κ is $(f_{v2} - f_w)c_{b1}\hat{v}^2/\kappa^2d^2$. Considering $f_{v2} - f_w$ is negative in the separated region (see Appendix), an increase in κ will enhance the turbulence source term and thus increase the Reynolds stress. The coefficient c_{b1} is positively correlated with the turbulence production term. Increasing c_{b1} will therefore raise the Reynolds stress level in the separation region. Finally, the coefficient c_{w2} alters f_w of the turbulence destruction term in different directions, which depends on the local flow quantities (see Appendix). The net

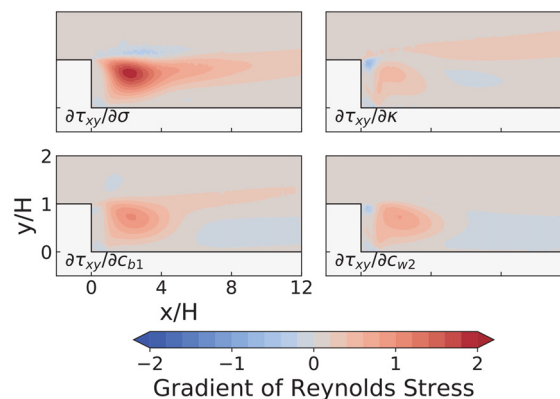


Fig. 11 Sensitivity of predicted Reynolds stress for backward-facing step

effect of c_{w2} contributes to an enhanced Reynolds stress level in this case.

The sensitivity analyses on predicting the Reynolds stress field of the bump flow are presented in Fig. 12. The Reynolds stress field is mainly governed by the physics of shock-induced separation. Increasing either coefficient of σ , κ , c_{b1} , and c_{w2} leads to a delayed shock front, which can be seen in Fig. 12(a) by the change of Reynolds stress in the vicinity of the shock front. Consequently, the separation size shrinks, and the Reynolds stress in

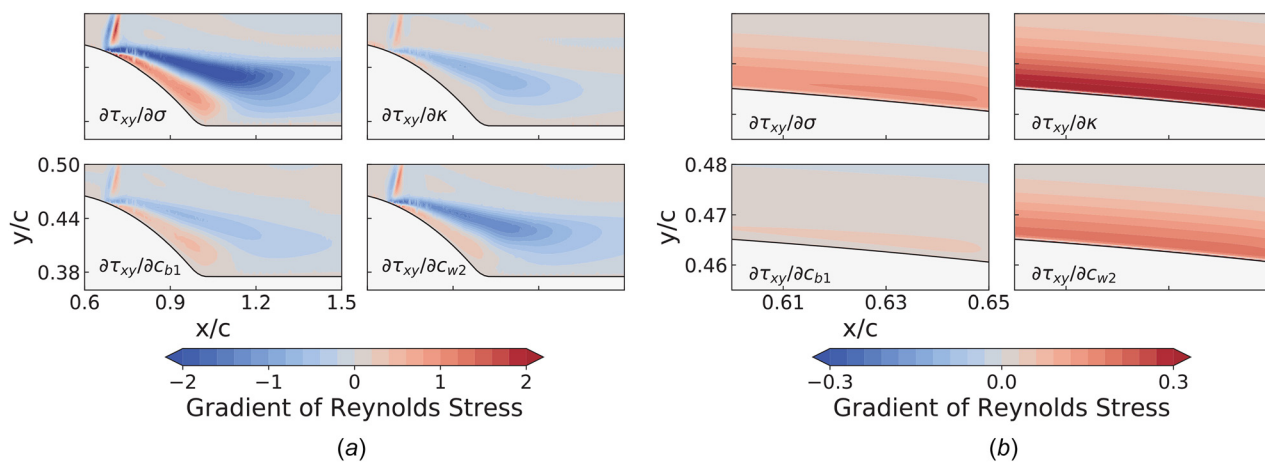


Fig. 12 Sensitivity of predicted Reynolds stress for axisymmetric transonic bump: (a) full view and (b) zoom-in view

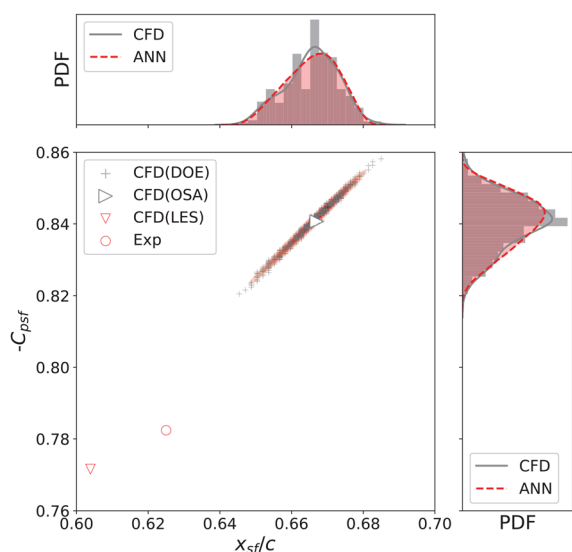


Fig. 13 Uncertainty of predicted shock front location (x_{sf}/c) and shock front pressure coefficient ($-C_{psf}$) (scatters: samples from experiment and CFD; contours: occurrence probability by ANN; experiment data: Ref. [28]; LES data: Ref. [30])

the separation region decreases. The delayed shock front is physically caused by a thickened preshock boundary layer. In the zoom-in view of Fig. 12(b), it is confirmed that the turbulence level near the preshock boundary layer increases with σ , κ , c_{b1} , and c_{w2} , which thickens the preshock boundary layer and eventually leads to the delay of the shock formation.

3.3 Uncertainty in Shock Prediction. The uncertainty on predicting the shock front location and pressure coefficient is illustrated in Fig. 13. In the main plot, the shock front location is plotted against the negative of the shock front pressure coefficient. The scatters represent experimental measurements or CFD results, and the contour illustrates the occurrence probability predicted by ANN. In the top and the right plots, the histogram represents the distribution of samples, and the curves are PDFs fitted by the kernel density estimation method [39] based on Gaussian kernels. It is observed that the SA model predicts a more downstream shock front location and a lower pressure coefficient at the shock front, indicating the deficiency of SA model in shock-capturing. Another observation is the apparent correlation between the shock front location and the shock front pressure coefficient. This is because

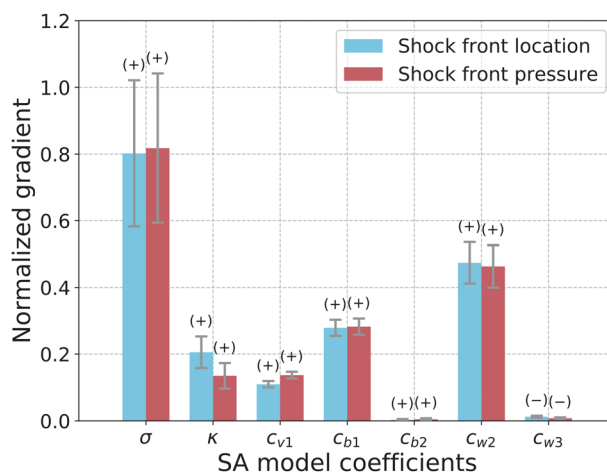


Fig. 14 Sensitivity of predicted shock front location (x_{sf}/c) and shock front pressure coefficient ($-C_{psf}$)

the preshock flow will experience an extended supersonic expansion if the shock is delayed.

The sensitivity analysis on shock prediction is given in Fig. 14. The mean value and the standard deviation of the normalized gradient over the investigated coefficient intervals are denoted by the bars and the error bars, respectively. It is found that increasing coefficients σ , κ , c_{v1} , c_{b1} , and c_{w2} leads to a delayed shock front, while c_{b2} and c_{w3} have negligible effects. Because the location and the pressure coefficient of the shock front are physically correlated, their sensitivity with respect to each SA model coefficient is similar to each other. These sensitive coefficients change the preshock boundary layer thickness and thus the shock location as was discussed in Sec. 3.2.

3.4 Uncertainty in Separation Prediction. The uncertainty on predicting the separation size is illustrated in Fig. 15. It is observed that the measured separation size of the step case is close to the prediction of the SA model, although the SA model cannot capture the velocity profile in the separated region accurately (i.e., Sec. I in Fig. 9(a)). However, the SA model predicts a smaller separation size in the bump case. Thus, the experiment dot falls out of the range of SA model results, and both separation sizes cannot be simultaneously captured accurately by tuning the SA model coefficients.

It was shown in Sec. 3.3 that the SA model predicts a delayed shock front, which may be the cause of the underpredicted shock-

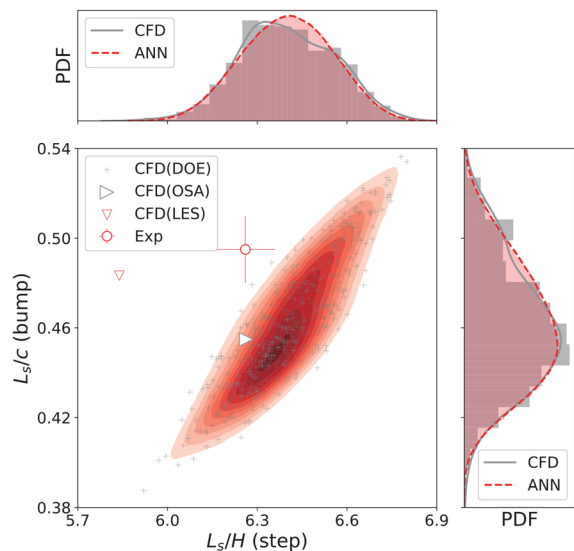


Fig. 15 Uncertainty of predicted separation size in the step (L_s/c) and the bump (L_s/H) case (scatters: samples from experiment and CFD; contours: occurrence probability by ANN; experiment data: Refs. [26] and [27]; LES data: Refs. [29] and [30])

induced separation size. In an attempt to elucidate this correlation, the shock front location is plotted against the separation size for the bump case in Fig. 16. It can be observed that the separation size does increase with the upstream movement of the shock front. However, fixing the shock front prediction by changing the SA model coefficients would lead to an overprediction of the separation size. Such a tradeoff effect further indicates the deficiency of the SA model in predicting both the shock and the separation.

The sensitivity analysis of the separation prediction is presented in Fig. 17. Regardless of the cause of separation, the separation size of the step case and the bump case has a similar trend with the SA model coefficients. Increasing σ , κ , c_{b1} , and c_{w2} or decreasing c_{w3} will reduce the separation size, while c_{v1} and c_{b2} have negligible effects. The separation size of the step case is determined by the reattachment location, which is physically

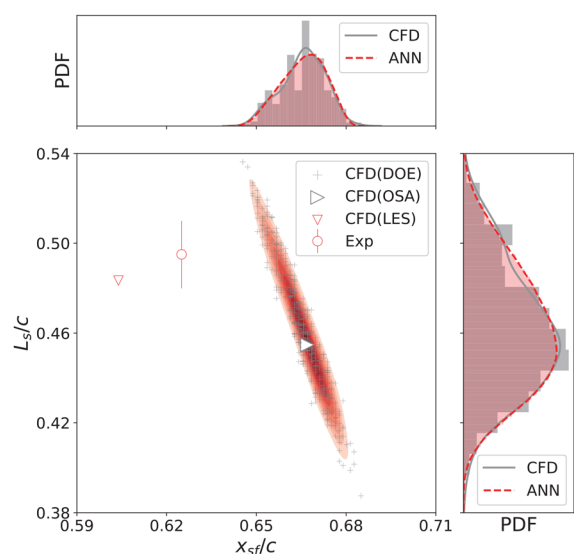


Fig. 16 Correlation between the shock front location (x_{sf}/c) and the separation size (L_s/c) (scatters: samples from CFD; contours: occurrence probability by ANN; experiment data: Ref. [28]; LES data: Ref. [30])

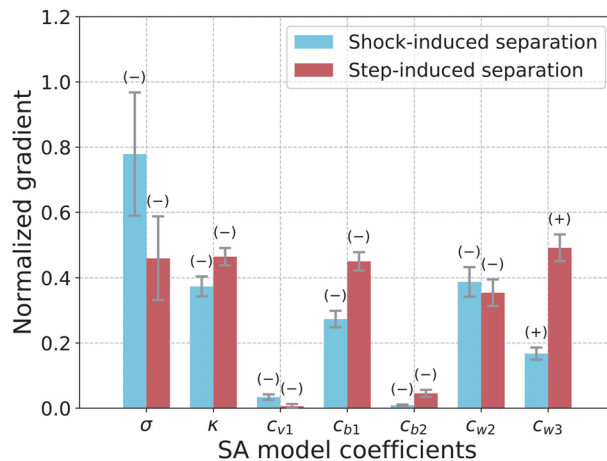


Fig. 17 Sensitivity of predicted separation size

correlated with the Reynolds stress magnitude. Since decreasing σ , κ , c_{b1} , and c_{w2} and increasing c_{w3} will reduce the Reynolds stress level in the separation region, they will increase the separation size due to a weaker turbulent mixing effect. The separation size of the bump case is determined by both the separation location and the reattachment location. In addition to the mechanisms related to the reattachment point, decreasing σ , κ , c_{b1} , and c_{w2} will move the shock front and the separation point toward upstream, and thus also increase the separation size.

4 Discussions and Outlook

4.1 Role of Diffusion Coefficient. From the above analyses, it is observed that the diffusion coefficient σ is the most sensitive coefficient. Since σ occurs both in the diffusion term and the destruction term, it is worth digging out which term plays the dominant role. To elucidate that, the coefficient σ has been split into σ_{des} in the destruction term and σ_{diff} in the diffusion term. A full factorial experiment with additional 25 samples is designed and tested in both cases by CFD. These samples differ in the values assigned to σ_{des} and σ_{diff} , while other coefficients are kept as the default values of the OSA model.

Contours of shock front location predicted by different sets of σ_{des} and σ_{diff} are presented in Fig. 18(a). Both terms have an equivalent effect on shock prediction as the contour is largely diagonal. This is because either term can change the near-wall Reynolds stress level and thus the preshock boundary layer thickness. For the separation prediction presented in Fig. 18(b), however, the source-related σ_{des} term is dominant over the σ_{diff} term as the isolines of the shock-induced separation size are almost vertical. Therefore, it is the total budget of Reynolds stress rather than its spatial distribution that controls the separation size.

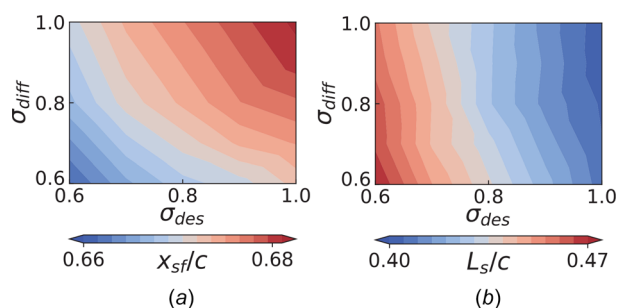


Fig. 18 Effect of σ_{des} and σ_{diff} on predicting (a) shock front location and (b) shock-induced separation size

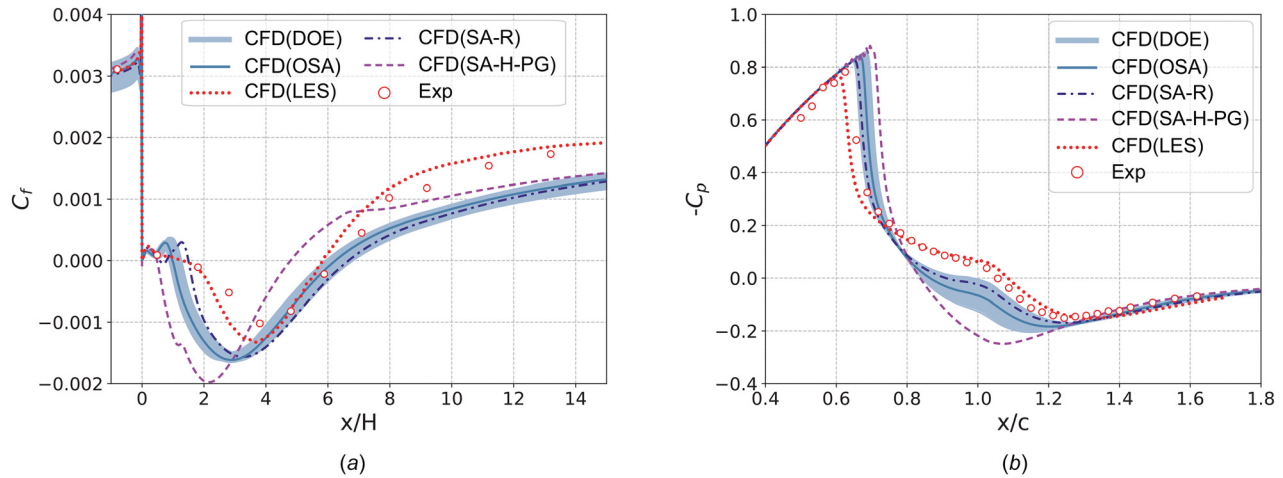


Fig. 19 Evaluation of modified Spalart–Allmaras turbulence model forms on predicting (a) C_f in backward-facing step and (b) C_p in axisymmetric transonic bump

4.2 Modifications on Model Form. It was established in the former studies that the SA model form is deficient in cases with rotation and curvature [40], secondary flows [41], pressure gradient [18], and 2D/3D flow separation [42–44]. From the perspective of the current UQ study, it is confirmed that the deficiency comes from separated flow modeling and the source terms were found significant. Several attempts to modify the SA model form have been made by using a combination of flow physics, intuition, and empiricism. In this section, two models modifying the production term of the SA model are evaluated, namely, the SA-H-PG model and the SA-R model. The SA-H-PG model boosts the turbulent viscosity in regions with helicity and adverse pressure gradient, which improves the prediction of compressor stall [45]. It should be noted that in the 2D flow cases studied in this paper, the helicity term is zero everywhere in the domain, and thus, only the adverse pressure gradient term is switched on. In contrast, the SA-R model reduces the turbulent viscosity in regions where vorticity exceeds strain rate, and it improves the prediction on wingtip vortex [46].

The predicted skin friction of the step case and pressure coefficient of the bump case are shown in Fig. 19. In general, none of these modified model forms can match up with the hi-fi results. The SA-H-PG model shows even worse results since it predicts excessive turbulent viscosity that leads to an underpredicted separation size in the step case and a delayed shock front in the bump case. The SA-R model shows slightly better results in the C_f distribution in the separated region and the shock front location, but the reattachment location of the step case is overpredicted.

The deficiency of the SA model and its variants arises from the empiricism in determining the model form, which involves human decisions made by considering a limited number of databases. With the accumulation of hi-fi turbulence data, a concurrent research direction is using machine learning to build data-driven turbulence models. Employing data-driven terms in either the transport equation or the Boussinesq approximation has yielded promising results in certain types of 2D flows [8]. For future modifications on the SA model form, it is recommended to train a data-driven source term considering hi-fi data across diverse flow regimes.

5 Conclusions

In this paper, a metamodel-based uncertainty quantification framework is presented. Using the established framework, the parametric uncertainty of the SA model coefficients for predicting simplified compressor flow features has been investigated.

The SA model successfully predicts velocity profiles and Reynolds stress profiles in wall-attached flows. In regions with shock or separation, however, the high-fidelity results of velocity profiles, Reynolds stress profiles, shock front, and separation size fall out of the parametric uncertainty band although the parametric uncertainty is larger in these regions than elsewhere in the domain. Such results indicate the limitation of the SA model in predicting transonic or separated flows.

It was found that Reynolds stress, shock, and separation predictions are sensitive to coefficients σ , κ , c_{b1} , and c_{w2} . Increasing either of these coefficients leads to a higher Reynolds stress level in the separation region, a more delayed shock front, and a smaller separation size. The coefficients κ , c_{b1} , and c_{w2} are directly linked to the source term. The coefficient σ in the destruction term plays a more important role in the separation prediction than its counterpart in the diffusion term, which demonstrates the significance of source term further.

Recalibration of model coefficients leads to contradictory results when considering multiple QoIs across flow regimes, such as the tradeoff effect between the shock front and the shock-induced separation size. This finding implies the need of a modified SA model form rather than recalibration of coefficients. The existing modified SA model forms do not show significant improvement in the investigated cases. For future research, the opportunity of improving the SA model accuracy by using a data-driven source term is pursued.

Funding Data

- Imperial College President Ph.D. Scholarship (No. 01015425).

Nomenclature

- c = bump chord length
- C_p = pressure coefficient
- C_{psf} = shock front pressure coefficient
- H = step height
- L_s = separation size
- M = Mach number
- $M(\cdot)$ = metamodel
- Re = Reynolds number
- \mathbf{x} = vector of input variables
- x_{sf} = shock front location
- ε = normalized error
- τ = Reynolds stress tensor

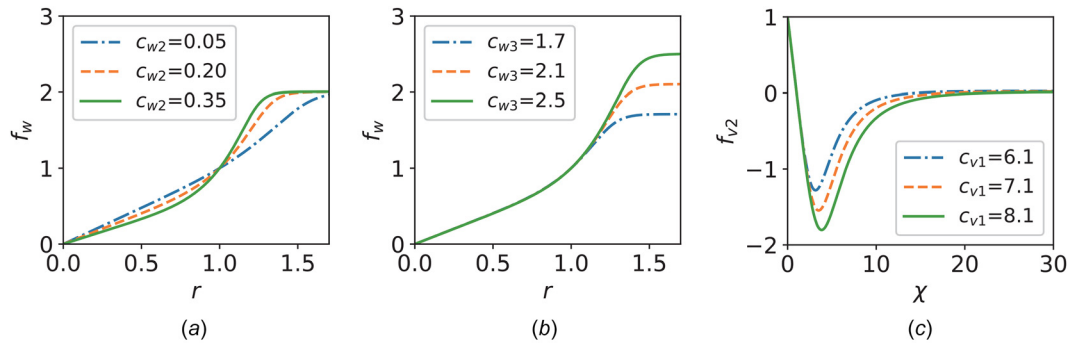


Fig. 20 Empirical functions in Spalart-Allmaras turbulence model: (a) f_w and c_{w2} , (b) f_w and c_{w3} , and (c) f_{v2} and c_{v1}

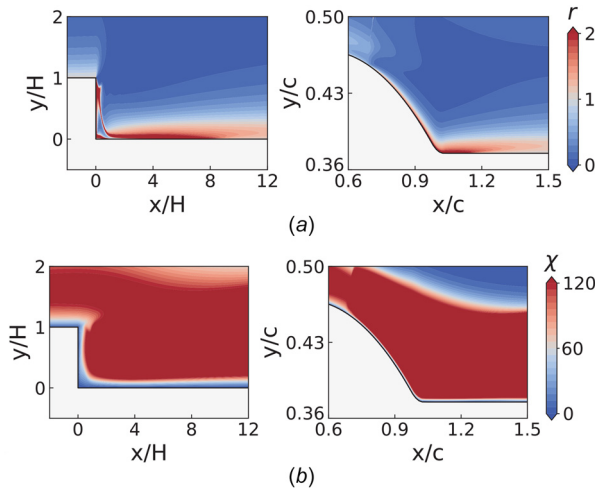


Fig. 21 Illustration of (a) r and (b) χ distribution

Appendix: Functions in Spalart-Allmaras Turbulence Model

The SA turbulence model uses empirical functions $f_w(r)$ and $f_{v2}(\chi)$ with coefficients c_{w2} , c_{w3} , and c_{v1} to calibrate the near-wall turbulence of wall-attached flows. The f_w function determines the turbulence destruction rate, and the f_{v2} function multiplied by χ controls the turbulence production term by changing the modified strain rate \hat{S} . In Fig. 20, these functions with different values of coefficients are plotted to help understand their behaviors.

The f_w function increases with r when r is small, and it turns to a constant equal to c_{w3} when r becomes large. The turning rate is controlled by c_{w2} : the larger the value of c_{w2} , the faster the f_w function turns. When $r \in (0, 1)$ (e.g., free shear flow, outer part of boundary layer, and near-wall region with favorable pressure gradient [1]), an increase in c_{w2} will decrease the turbulence destruction, but c_{w3} does not have any effects. When $r \in (1, +\infty)$ (e.g., near-wall region with adverse pressure gradient [1]), an increase in c_{w2} or c_{w3} will enhance the turbulence destruction. An example of r distribution is given in Fig. 21(a), where the near-wall value of r is large but the far-wall value is small.

The f_{v2} function decreases with χ to negative values first, and then, gradually increases back to zero. The minimum value of f_{v2} is negatively correlated with c_{v1} . Thus, increasing c_{v1} reduces the local turbulence production when $\chi \in (1, 30)$. The distribution of χ is illustrated in Fig. 21(b), where the near-wall value of χ is small but the far-wall value is large.

References

- [1] Spalart, P., and Allmaras, S., 1994, "A One-Equation Turbulence Model for Aerodynamic Flows," *Rech. Aerosp.*, **1**, pp. 5–21.
- [2] Zhao, F., Dodds, J., and Vahdati, M., 2018, "Poststall Behavior of a Multistage High Speed Compressor at Off-Design Conditions," *ASME J. Turbomach.*, **140**(12), p. 121002.
- [3] Dodds, J., and Vahdati, M., 2015, "Rotating Stall Observations in a High Speed Compressor—Part II: Numerical Study," *ASME J. Turbomach.*, **137**(5), p. 051003.
- [4] Gourdain, N., Burguburu, S., Leboeuf, F., and Michon, G. J., 2010, "Simulation of Rotating Stall in a Whole Stage of an Axial Compressor," *Comput. Fluids*, **39**(9), pp. 1644–1655.
- [5] Pullan, G., Young, A. M., Day, I. J., Greitzer, E. M., and Spakovszky, Z. S., 2015, "Origins and Structure of Spike-Type Rotating Stall," *ASME J. Turbomach.*, **137**(5), p. 51007.
- [6] Denton, J. D., 2010, "Some Limitations of Turbomachinery CFD," *ASME Paper No. GT2010-22540*.
- [7] Day, I. J., 2016, "Stall, Surge, and 75 Years of Research," *ASME J. Turbomach.*, **138**(1), p. 011001.
- [8] Duraisamy, K., Iaccarino, G., and Xiao, H., 2019, "Turbulence Modeling in the Age of Data," *Annu. Rev. Fluid Mech.*, **51**(1), pp. 357–377.
- [9] Godfreyand, A., and Cliff, E., 2001, "Sensitivity Equations for Turbulent Flows," *AIAA Paper No. 2001-1060*.
- [10] Xiao, H., and Cinnella, P., 2019, "Quantification of Model Uncertainty in RANS Simulations: A Review," *Prog. Aerosp. Sci.*, **108**, pp. 1–31.
- [11] Han, D., and Hosder, S., 2014, "Inherent and Epistemic Uncertainty Analysis for Computational Fluid Dynamics Simulations of Synthetic Jet Actuators," *Int. J. Uncertain. Quantif.*, **4**(6), pp. 511–533.
- [12] Schaefer, J., Hosder, S., West, T., Rumsey, C., Carlson, J. R., and Kleb, W., 2017, "Uncertainty Quantification of Turbulence Model Closure Coefficients for Transonic Wall-Bounded Flows," *AIAA J.*, **55**(1), pp. 195–213.
- [13] Schaefer, J., Cary, A., Mani, M., Krakos, J., and Hosder, S., 2018, "Grid Influence on Turbulence Model Coefficient Uncertainties in Transonic Wall-Bounded Flows," *AIAA J.*, **56**(8), pp. 3123–3137.
- [14] Stephanopoulos, K., Whitte, I., Wray, T., and Agarwal, R. K., 2018, "Uncertainty Quantification of Turbulence Model Coefficients in OpenFOAM and Fluent for Mildly Separated Flows," *AIAA Paper No. 2018-3553*.
- [15] Oliver, T. A., and Moser, R. D., 2011, "Bayesian Uncertainty Quantification Applied to RANS Turbulence Models," *J. Phys. Conf. Ser.*, **318**(4), p. 042032.
- [16] Kato, H., and Obayashi, S., 2013, "Approach for Uncertainty of Turbulence Modeling Based on Data Assimilation Technique," *Comput. Fluids*, **85**, pp. 2–7.
- [17] Cheung, S. H., Oliver, T. A., Prudencio, E. E., Prudhomme, S., and Moser, R. D., 2011, "Bayesian Uncertainty Analysis With Applications to Turbulence Modeling," *Reliab. Eng. Syst. Safety*, **96**(9), pp. 1137–1149.
- [18] Edeling, W. N., Cinnella, P., and Dwight, R. P., 2014, "Predictive RANS Simulations Via Bayesian Model-Scenario Averaging," *J. Comput. Phys.*, **275**, pp. 65–91.
- [19] Papadimitriou, D. I., and Papadimitriou, C., 2015, "Bayesian Uncertainty Quantification of Turbulence Models Based on High-Order Adjoint," *Comput. Fluids*, **120**, pp. 82–97.
- [20] Cumpsty, N. A., 1989, *Compressor Aerodynamics*, Longman Scientific and Technical, Harlow, UK.
- [21] You, D., Wang, M., Moin, P., and Mittal, R., 2007, "Large-Eddy Simulation Analysis of Mechanisms for Viscous Losses in a Turbomachinery Tip-Clearance Flow," *J. Fluid Mech.*, **586**, pp. 177–204.
- [22] Babinsky, H., and Harvey, J. K., 2011, *Shock Wave-Boundary-Layer Interactions*, Cambridge University Press, Cambridge, UK.
- [23] Puterbaugh, S. L., and Copenhaver, W. W., 1997, "Flow Field Unsteadiness in the Tip Region of a Transonic Compressor Rotor," *ASME J. Fluids Eng.*, **119**(1), pp. 122–128.
- [24] Gannon, A. J., and Hobson, G. V., 2009, "Pre-Stall Instability Distribution Over a Transonic Compressor Rotor," *ASME J. Fluids Eng.*, **131**(5), p. 051106.

- [25] Hah, C., and Shin, H. W., 2012, "Study of Near-Stall Flow Behavior in a Modern Transonic Fan With Compound Sweep," *ASME J. Fluids Eng.*, **134**(7), p. 071101.
- [26] Driver, D. M., and Seegmiller, H. L., 1985, "Features of a Reattaching Turbulent Shear Layer in Divergent Channel Flow," *AIAA J.*, **23**(2), pp. 163–171.
- [27] Horstman, C., and Johnson, D., 1984, "Prediction of Transonic Separated Flows," *AIAA J.*, **22**(7), pp. 1001–1003.
- [28] Bachalo, W. D., and Johnson, D. A., 1986, "Transonic, Turbulent Boundary-Layer Separation Generated on an Axisymmetric Flow Model," *AIAA J.*, **24**(3), pp. 437–443.
- [29] Probst, A., Lowe, J., Reu, S., Knopp, T., and Kessler, R., 2016, "Scale-Resolving Simulations With a Low-Dissipation Low-Dispersion Second-Order Scheme for Unstructured Flow Solvers," *AIAA J.*, **54**(10), pp. 2972–2987.
- [30] Uzun, A., and Malik, M., 2019, "Wall-Resolved Large-Eddy Simulations of Transonic Shock-Induced Flow Separation," *AIAA J.*, **57**(5), pp. 1–18.
- [31] Sayma, A. I., Vahdati, M., Sbardella, L., and Imregun, M., 2000, "Modeling of Three-Dimensional Viscous Compressible Turbomachinery Flows Using Unstructured Hybrid Grids," *AIAA J.*, **38**(6), pp. 945–954.
- [32] Hirsch, C., 1990, *Numerical Computation of Internal and External Flows, Volume 2: Computational Methods for Inviscid and Viscous Flows*, Wiley, Chichester, UK.
- [33] Rumsey, C. L., *Turbulence Modeling Resource*, NASA Langley Research Center, Hampton, VA, accessed Nov. 8, 2018, <https://turbmodels.larc.nasa.gov/>
- [34] McKay, M. D., Beckman, R. J., and Conover, W. J., 1979, "Comparison of Three Methods for Selecting Values of Input Variables in the Analysis of Output From a Computer Code," *Technometrics*, **21**(2), pp. 239–245.
- [35] Ling, J., Kurzwski, A., and Templeton, J., 2016, "Reynolds Averaged Turbulence Modelling Using Deep Neural Networks With Embedded Invariance," *J. Fluid Mech.*, **807**, pp. 155–166.
- [36] Lu, H., Li, Q., and Pan, T., 2016, "Optimization of Cantilevered Stators in an Industrial Multistage Compressor to Improve Efficiency," *Energy*, **106**, pp. 590–601.
- [37] Liu, Y., Dinh, N., Sato, Y., and Niceno, B., 2018, "Data-Driven Modeling for Boiling Heat Transfer: Using Deep Neural Networks and High-Fidelity Simulation Results," *Appl. Therm. Eng.*, **144**, pp. 305–320.
- [38] Nocedal, J., and Wright, S. J., 2006, *Numerical Optimization*, Springer, New York.
- [39] Silverman, B. W., 1998, *Density Estimation for Statistics and Data Analysis*, Taylor & Francis Group, New York.
- [40] Shur, M. L., Strelets, M. K., Travin, A. K., and Spalart, P. R., 2000, "Turbulence Modeling in Rotating and Curved Channels: Assessing the Spalart-Shur Correction," *AIAA J.*, **38**(5), pp. 784–792.
- [41] Spalart, P. R., 2000, "Strategies for Turbulence Modelling and Simulations," *Int. J. Heat Fluid Flow*, **21**(3), pp. 252–263.
- [42] Hirsch, C., and Tartinville, B., 2009, "Reynolds-Averaged Navier-Stokes Modelling for Industrial Applications and Some Challenging Issues," *Int. J. Comput. Fluid Dyn.*, **23**(4), pp. 295–303.
- [43] Rumsey, C. L., and Swanson, R. C., 2009, "Turbulence Modelling for Active Flow Control Applications," *Int. J. Comput. Fluid Dyn.*, **23**(4), pp. 317–326.
- [44] Liu, Y., Lu, L., Fang, L., and Gao, F., 2011, "Modification of Spalart-Allmaras Model With Consideration of Turbulence Energy Backscatter Using Velocity Helicity," *Phys. Lett. A*, **375**(24), pp. 2377–2381.
- [45] Lee, K. B., Wilson, M., and Vahdati, M., 2018, "Validation of a Numerical Model for Predicting Stalled Flows in a Low-Speed Fan—Part I: Modification of Spalart-Allmaras Turbulence Model," *ASME J. Turbomach.*, **140**(5), p. 051008.
- [46] Dacles-Mariani, J., Zilliac, G. G., Chow, J. S., and Bradshaw, P., 1995, "Numerical/Experimental Study of a Wingtip Vortex in the Near Field," *AIAA J.*, **33**(9), pp. 1561–1568.